AIAA-2000-0134
Advanced Turbulence Model for Transitional and Rotational Flows in Turbomachinery

Hsin-Hua Tsuei

Concepts, ETI, Inc.

White River Junction, VT

and

J. Blair Perot

Dept. of Mechanical and Industrial Engineering

University of Massachusetts

Amherst, MA

AIAA-2000-0134

ADVANCED TURBULENCE MODEL FOR TRANSITIONAL AND ROTATIONAL FLOWS IN TURBOMACHINERY

Hsin-Hua Tsuei[*]
Concepts ETI, Inc.
White River Junction, VT
and
J. Blair Perot[†]
Dept. of Mechanical and Industrial Engineering
University of Massachusetts
Amherst, MA

INTRODUCTION

Turbulence Modeling for CFD

Computational Fluid Dynamics (CFD) for aircraft engine and airframe design is now commonplace. Practical CFD calculations require models for approximating the effects of turbulent flow structure. Many turbulence models have been developed, but the need for more robust, computationally efficient, and easy-to-use turbulence models applicable to wide classes of aerodynamic and aerothermodynamic flow problems has been well established. Turbomachinery flows include a variety of complex flow phenomena, including laminar-to-turbulent transition and relaminarization, adverse pressure gradients, flow separation, secondary flow mixing, rotor-stator interaction, tip clearance flows, combustion, and heat transfer. Each of these flow characteristics must be taken into account in turbomachinery engineering. A common thread among all these phenomena is turbulence. Turbulence is taken into account in today's engineering calculations through the use of turbulence models. However, current commonly used turbulence models perform relatively poorly in predicting certain types of turbomachinery flows, especially in flows experiencing transition and rotation. For example, the widely used k-ε turbulence model always underpredicts the transition. Today's turbulence models can be adjusted to obtain a fairly accurate solution for certain types of flows, though success typically depends on the skill of the fluid dynamics expert who must "tweak" the modeling using ad hoc damping functions or manipulations of the turbulence modeling parameters. It is highly desirable to have a powerful, generalized turbulence model which accurately models the full range of turbulence effects across a wide range of common turbomachinery flows without substantial user interaction.

Turbulence modeling is an ongoing area of research and there have been many claims of improved turbulence models which have later disappointed users. Past efforts at improved turbulence modeling have historically failed because they improved accuracy only for a specific flow condition, such as shear, vortex flow, etc. These new turbulence models were not generalized to work under a wide variety of flow conditions. Without detailed knowledge on the part of the user of the models' formulation, plus additional tweaking for each specific application, substantial improvements in accuracy usually could not be achieved. In addition, many of these more complex models incurred a major penalty in computer memory use and computation time as a result of going to a two- or three-equation formulation, while not providing sufficient improvement in accuracy over the less demanding models to justify this increased computation time. In addition, most researchers, despite the fairly substantial nature of some of the past efforts, have failed to confirm their models with basic testing and first-principles techniques.

---

[*] Senior CFD/Project Engineer. AIAA member.

[†] Assistant Professor. AIAA member.

Despite attempting to capture complex flow field physics, such as recirculating regions, shock-wave boundary layer interactions, horseshoe vortices, 3D boundary layers, secondary flow effects, tip clearance flows, and rotation and curvature effects, all the existing turbulence models fail to predict transition occurring in turbomachinery flows (Hirsch[1]). Therefore, ensuring the reliability of numerical predictions is crucial to turbomachinery engineering design. There are a variety of turbulence models available, ranging from algebraic models to Reynolds Stress Transport Equation (RSTE) models. Within each family, based on different assumptions or on different empirical data, even larger numbers of variants have been derived. The proper setup and calibration of turbulence models can be a critical role in today's practical CFD applications since none of the available models offer universal validity. On the contrary, all of them are based, to a greater or lesser degree, on empirical techniques. More advanced turbulence models, like the RSTE, or the Large Eddy Simulation (LES), are capable of capturing complex 3D turbulent flow physics but at an unacceptable cost in computer memory requirements and computational cost.

The algebraic models, such as Baldwin-Lomax, and one- or two-equation models, such as k-ε are based on the eddy viscosity hypothesis, which assumes that the Reynolds stress is a function of the mean flow strain rate, with isotropic turbulence exchanges similar to the molecular viscosity. Algebraic models are widely used in CFD codes because of their simplicity and low computational cost. No additional transport equations are required to be coupled with the Navier-Stokes equations. The version developed by Baldwin-Lomax[2] is the most popular of the algebraic turbulence models. The Baldwin-Lomax model assumes that the turbulent layer is formed by two regions, an inner and an outer region, with different expressions for the eddy viscosity coefficient under the assumption of isotropic turbulence. However, because the Baldwin-Lomax model is not able to take into account the transport and diffusion of turbulence, difficulty arises in the vicinity of separation or reattachment points. However, it is generally considered that algebraic models provide acceptable results for attached boundary layers, especially for external applications.

Applications of the Baldwin-Lomax model to turbomachinery flow problems were reported and summarized by Hirsch[1] and Dawes[3], and the discrepancies between the measured data and the predicted results were documented. An attempt was reported by Nakahashi[4] to apply the Baldwin-Lomax model to predict transition in a turbine cascade by introducing a transition criterion based on the maximum eddy viscosity exceeding a preset value. At a high incidence angle and a high Mach number, the transition was underpredicted, leading to an inaccurate global flow field when compared to Schlieren pictures, primarily because of the presence of a separated flow region induced by shock-wave boundary layer interactions.

A variety of two-equation models has been developed over the years, the most popular being the k-ε model. The k-ε was developed by Launder and Spalding[5], and solves the transport equations of turbulent kinetic energy and dissipation rate. These two equations have to be computed simultaneously with the 3D Navier-Stokes equations. Various forms of the k-ε model are available, with the differences between the various versions being the treatment of near-wall low Reynolds number turbulence. The first attempt to apply the two-equation k-ε model to turbomachinery flows was pioneered by Hah[6], and an acceptable compromise between the range of validity and the required computation time was made. Prediction of 3D non-isotropic turbulence remains one of the model's deficiencies. Application of the k-ε model to various turbomachinery flows, such as a subsonic turbine blade and a transonic compressor, were performed by Matsuo[7], and Jennions and Turner[8]. Transition was also modeled using the k-ε model as noted by Savill[9]. The application of the k-ε model to transition required that a high free steam turbulence be imposed, which led to calculations predicting transitions prematurely. It was found that imposing a high upstream turbulence level to trigger transition led to the turbulence kinetic energy dissipating into the boundary layer more quickly than occurs in real flows. Another extreme case in which the k-ε model failed dramatically was the prediction of an impinging jet on a plate as described in Leschziner and Launder[10]. It appeared that the linear eddy viscosity stress-strain relation caused excessive levels of turbulent kinetic energy and eddy viscosity compared to the measured data. This result is significant for turbomachinery flows since a stagnation point always exists near the leading edge of a blade. Heat transfer at the leading edge is also poorly predicted today.

The more advanced RSTE models take into account the effects of anisotropy, rotation, and curvature (Mansour, Kim, and Moin[11]). They are able to capture 3D turbulent flow physics much better than the algebraic or the two-equation models. The drawback is that these models require a total of seven transport equations to be calculated for the Reynolds stress tensor and Navier-

Stokes equations. In addition, some implementations of these models have proven numerically "stiff" and, consequently, computationally unstable. These models need to be further developed before they can be applied to practical modeling of turbulence in turbomachinery.

In summary, although substantial work has been performed in the area of turbulence modeling, the search for a reliable and economical turbulence model for turbomachinery continues. The current turbulence model is expected to capture the full details of 3D non-isotropic turbulence and has the potential to more accurately model transition in a wide variety of flows. This greater accuracy is expected to be achieved with a computational cost similar to an enhanced k-ε model while providing detailed Reynolds stress information for the mean flow.

Types of Turbulence Models

There are a number of different types of turbulence models already available, including algebraic models, one- or two-equation models, Reynolds Stress Transport Equation (RSTE) models, and the Large Eddy Simulation (LES). Each of these models predicts satisfactorily accurate results for certain cases. However, a turbulence model having universal validity is still lacking. In today's competitive environment, turbomachinery designers must work effectively within even shorter product design cycles, requiring fast run times and efficient design tools. As a result, the algebraic models (such as the popular Baldwin-Lomax model) and the two-equation turbulence models (particularly the k-ε model) have been widely incorporated into CFD tools for both government and industry. These two models generally require less demanding computational resources and are able to provide reasonably accurate results in a reasonably timely fashion. However, the Baldwin-Lomax algebraic turbulence model often leads to unrealistic predictions for some types of flows commonly found in turbomachinery, such as flow in recirculating regions, secondary flows, shock-wave boundary layer interactions, etc. The two-equation k-ε model generally provides a better solution than the Baldwin-Lomax model, but it still lacks accuracy for transition and rotating flows. More advanced turbulence models, such as the RSTE or the LES, although capable of modeling more complicated turbulent flows (particularly for non-isotropic turbulence), often require prohibitive computation time. These advanced turbulence models are still in the academic development stage and require additional refinement before they can be beneficial for practical product design cycles. A reliable and accurate turbulence model is desired which combines the

advantages of the fast run time of algebraic or two-equation models and the non-isotropic, complex turbulent flow prediction capability of the more advanced turbulence models.

The present advanced turbulence model is based on a set of partial differential equations with theoretical procedures and boundary conditions formulated for a new set of two turbulence variables. This model was developed by Perot[12],[13]. The current technique models the scalar and vector potentials of the turbulent body force, rather than the Reynolds stress tensor or eddy viscosity. This approach has an advantage over eddy viscosity models (such as Baldwin-Lomax, k-ε, q-ω, etc.) in that no constitutive relationship between the Reynolds stress tensor and the mean velocity gradients needs to be hypothesized. (This advantage allows the possibility of a strong disequilibrium between the turbulence and the mean flow, such as has been shown to occur in rotating flows.) The present turbulence model also has an advantage over the RST equation models in that the same turbulent flow physics can be captured with a significant reduction in model closure complexity and associated computational cost. Due to its relative computational simplicity, the present model will be more robust than RSTE models and better able to account for wall and surface effects, yet has a computational cost similar to that of many "enhanced" two-equation models, which often add one, and more often two, additional partial differential equations.

THEORETICAL FORMULATION AND MODEL IMPLEMENTATION FOR COMPRESSIBLE TURBOMACHINERY FLOWS

For the sake of simplicity, incompressible, isothermal flow, the Reynolds Averaged Navier-Stokes (RANS) equations can be written as:

$$\frac{\partial \mathbf{u}}{\partial t} + \nabla \cdot (\mathbf{uu}) = -\nabla p + \nabla \cdot \nu \nabla \mathbf{u} - \nabla \cdot \mathbf{R} \qquad (1a)$$

$$\nabla \cdot \mathbf{u} = 0 \qquad (1b)$$

where u is the mean velocity vector, p is pressure, ν is the kinetic viscosity, and $\mathbf{R} = \mathbf{u'u'}$ is the Reynolds stress tensor. The Reynolds tensor represents the correlation of the fluctuating velocity components with four components for two-dimensional flows and nine components for 3D flows. The fundamental goal of RANS models is to hypothesize a relationship between this tensor and the mean flow variables so that Equations (1a) and (1b) can be solved. The same principles exist for the general (compressible) RANS equations.

The key to developing a model which avoids the use of a constitutive assumption, and yet does not involve the complexity of the full Reynolds stress transport closure used in the existing RANS models, is to focus on the fact that the Reynolds stresses actually contain more information than is required to calculate the mean flow. Only the divergence of the Reynolds stress tensor (a body force vector) is needed to evaluate the mean flow, so the remaining (non-equilibrium) terms can be neglected. A new set of turbulent variables was developed to model the scalar and vector potentials of the turbulent body force, rather than the Reynolds stress tensor or an eddy viscosity. The turbulent potentials (ϕ and ψ) are defined mathematically by the following equations.

$$\nabla^2 \phi + \nabla \times \psi = \nabla \cdot R \qquad (2a)$$

$$\nabla \cdot \psi = 0 \qquad (2b)$$

The second equation is a constraint on the vector potential. These equations can be rewritten to express the turbulent potentials explicitly.

$$\nabla^2 \phi = \nabla \cdot (\nabla \cdot R) \qquad (3a)$$

$$-\nabla^2 \psi = \nabla \times (\nabla \cdot R) \qquad (3b)$$

The boundary conditions on these equations are constructed intuitively. Both potentials are required to go to zero at infinity, at a wall, or at a free surface. Note that by definition (Equation 2a) the scalar potentials are those portions of the turbulence that contribute to the mean pressure but do not affect the mean vorticity, or vorticity of the mean flow, ($\omega = \nabla \times u$). Only the vector potential has the ability to affect the mean vorticity, and it only transports vorticity; it does not create or destroy vorticity.

In flows with a single inhomogeneous direction (say the y-direction), Equations 3a and 3b simplify to $\phi = R_{22}$, $\psi_1 = -R_{23}$, $\psi_2 = 0$, $\psi_3 = R_{12}$. For this reason, it is also reasonable to view the vector potentials as a conceptual generalization of the shear stress (u´v´) to arbitrary geometries and three dimensions. These relations will be used in evaluating model predictions against experimental data and against Reynolds stress data from published Direct Numerical Solution (DNS) data.

In two-dimensional (2D) flow, the vector potential is aligned perpendicular to the flow and has only a single nonzero component (ψ_3). In full 3D flow, the vector potential must obey the divergence free constraint. This implies that the vector potential can be computed, even

in 3D flows, with a cost roughly equivalent to the scalar potential. Therefore, the overall complexity and associated computational cost of solving a model for the proposed turbulent potentials should be roughly less than half of that of a full Reynolds stress closure.

The transport equations for the turbulent potentials were derived by Perot (1995,1997):

$$\frac{D\phi}{Dt} = \nabla \cdot (\nu + \nu_T / \sigma_\phi) \nabla \phi + P_\phi + D_\phi \qquad (4a)$$

$$\frac{D\psi}{Dt} = \nabla \cdot (\nu + \nu_T / \sigma_\psi) \nabla \psi + P_\psi + D_\psi \qquad (4b)$$

where P_ϕ, P_ψ represent the production terms for the turbulent potentials, and D_ϕ, D_ψ are the dissipation terms, respectively.

The general modeling philosophy is to use existing Reynolds stress transport models, and the assumption of a single inhomogeneous direction, to guide the construction of the turbulent potential source terms. Other guiding factors have been the construction of a model that naturally obtains the correct asymptotic behavior near walls and free surfaces, and a model which corresponds correctly to shearing, both initially and in the long time limit. Obtaining the correct rapid response for shear flows is important because this situation is closely related to many engineering applications. Examples are the freestream turbulence which suddenly encounters an obstacle, such as a blade in turbomachinery, and the initial development of tripped boundary layers and free shear layers.

The turbulent potential transport equations are supplemented by transport equations for the turbulent kinetic energy and the dissipation. These equations were chosen because they are widely used for engineering solutions, and because data for both k and ε are widely available. These equations enable the system to behave correctly in time developing or convection dominated situations, and help to make the equations system more robust in situations where the mean flow gradients are small. Other two-equation models, such as k/ω and k/L models could easily be substituted if they were preferred.

The turbulent potential model was integrated into the BTOB3D turbomachinery CFD code. The BTOB3D code was developed by Prof. W. Dawes[14], of Cambridge University, for general 3D centrifugal and axial turbomachinery flows. The turbulence model implemented in the BTOB3D code is the algebraic Baldwin-Lomax model. This particular CFD code is

American Institute of Aeronautics and Astronautics

widely used in the turbomachinery industry around the world and is popular for its fast solution times, which have helped make CFD a practical tool for daily design optimization.

FUNDAMENTAL VALIDATIONS

A series of fundamental benchmark turbulent flow cases for model validation is finished. This model has successfully demonstrated the ability to predict a turbulent channel flow at different Reynolds numbers, transition and relaminarization of a channel flow, a rotating channel flow, a turbulent mixing layer, and a turbulent boundary layer with adverse pressure gradient. With these promising features, which are specifically applicable for turbomachinery flows, it is proposed to further develop this turbulence model to extend its applicability to all types of turbomachinery, including compressors, turbines, and pumps, to provide accurate engineering solutions. Several representative benchmark test results, of particular interest for turbomachinery flow predictions, are presented below using the turbulent potential model. It should be noted that turbomachinery flows are some of the most complex flows to model. Therefore, it is reasonable to assume that a turbulence model developed and proven effective for turbomachinery applications will be widely applicable to other types of flow as well.

Rotation Prediction

Rotation is an integral part of turbomachinery and cannot be ignored when developing a general turbulence model. Rotation produces a Coriolis force that can be coupled with the turbulence and affects machine performance. At a first level of approximation, a turbulent eddy acts like a gyroscope with individual angular momentum. When rotation is imposed, turbulent eddies try to maintain their angular momentum to balance the rotation. This process alters eddy orientation, and hence, influences the conventional turbulence structure, leading to a reduction of turbulent dissipation rate and the creation of non-isotropic flows. The turbulent potential model shows correct qualitative predictions due to rotation. Figure 1 shows the model prediction results for rotating channel flow. The Reynolds number is 7,900. The results are shown across the entire channel since the flow is no longer symmetric about the centerline. The proposed model correctly predicts the qualitative effects of stabilization on the upper wall and enhanced turbulence production on the lower wall.
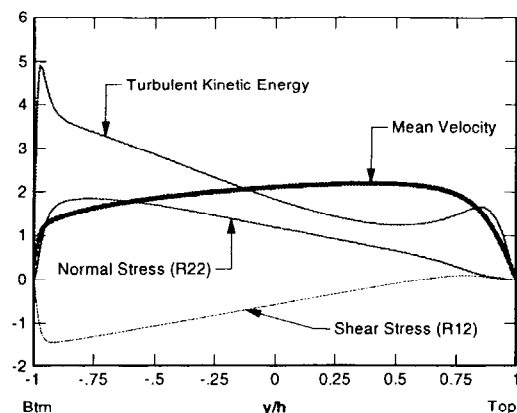

Figure 1. Predictions, using the turbulent potential model, of streamwise variation of flow parameters for rotating channel flow, $Re = 7,900$.

Prediction of a Boundary Layer with an Adverse Pressure Gradient

Adverse pressure gradient boundary layers represent a situation where the classic turbulence modeling assumptions are not well approximated. In particular, the turbulence is not in equilibrium with the mean flow, which violates the eddy viscosity hypothesis. However, such flows of adverse pressure (diffusing flows) are at the heart of turbomachinery. Two-equation models tend to have some problems predicting adverse pressure boundary layers. However, models which predict shear stress directly (Johnson and King[15], and Bradshaw, Ferris and Atwell[16], and full Reynolds stress closure) generally show considerable more success with these types of flows. Since the proposed model also directly predicts a quantity similar to shear stress, it is expected to perform well in these situations.

Figure 2 shows the computed streamlines for the adverse pressure gradient experiment of Samual and Joubert[17]. The vertical direction has been exaggerated by a factor of ten to highlight the rapid growth of the boundary layer under the influence of an adverse pressure gradient. The predicted friction coefficient as a function of the downstream distance is shown in Figure 3. Circles indicate the experimental data and the solid line represents the numerical prediction. It is apparent that the agreement between the experimental data and the predicted results is very good. Most two-equation models tend to underpredict the friction coefficient as separation is approached, leading to calculations which predict separation prematurely.

American Institute of Aeronautics and Astronautics

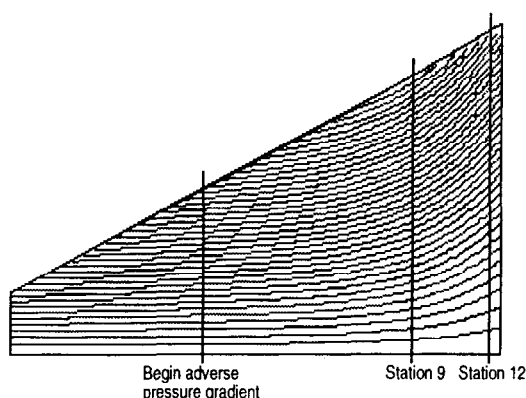Begin adverse
pressure gradient

Station 9   Station 12

Figure 2. Computed streamlines for an adverse pressure gradient boundary layer. Note that the vertical coordinate has been expanded by a factor of ten.
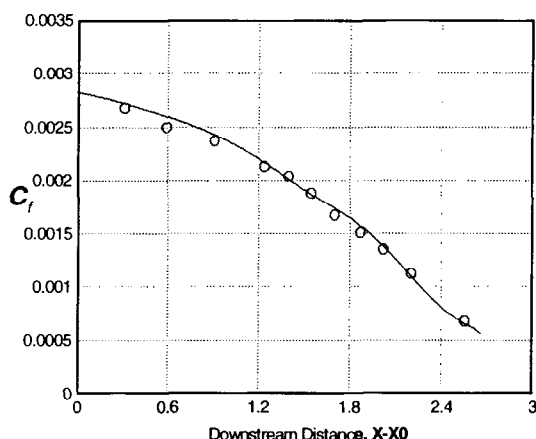

Figure 3. Measured and predicted friction coefficient versus downstream distance for an adverse pressure gradient boundary layer.

ADVANCED MODEL VALIDATIONS AGAINST DNS AND LASER VELOCIMETRY DATA

Prediction of Fully Developed Turbulent Channel Flow

The turbulent potential model was further validated against a published DNS data for a fully developed turbulent channel flow. The DNS computation was conducted by Moser, Kim and Mansour[18]. The Reynolds number of the fully developed channel flow was 8,000, based on the half channel width. The number of grid points used in the DNS simulation was on the order of 10,000,000, a very large number of grid such that the computation can only be carried out on a supercomputer. By computing the fully developed channel flow and compared with DNS data, the results implied the accuracy of the turbulent potential models

for predicting turbulent production, dissipation rate, and other turbulent transport quantities like cross product of the Reynolds stresses.

The current computation using the turbulent potential model was performed on a 59 x 97 mesh system, a significant reduction in grid size compared to the DNS calculation. The mesh is stretched toward the wall and represents a grid system of the first grid point well into the viscous layer region, y+ < 1.0. Figure 4 showed the non-dimensionalized fully developed velocity profiles for the turbulent potential model and the DNS data. The radial direction was also non-dimensionalized by the half channel width. Excellent agreement was observed between the turbulent potential model results and the DNS data. These velocity profiles literally coincided with each other. Detailed turbulent transport properties will be discussed in the following paragraphs.
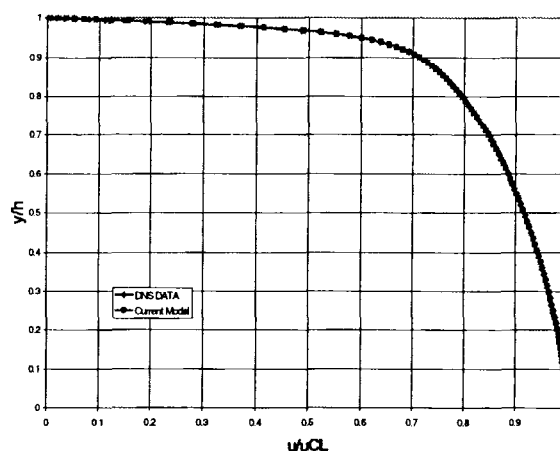

Figure 4. Velocity profile compared to DNS data.

Figure 5 shows the non-dimensionalized turbulent kinetic energy profiles. As can be seen from this figure, the turbulent potential model compared very well near the channel centerline to the log layer, almost agreed with the DNS data exactly. The location of the peak of TKE agreed well with the DNS data (y+ ~ 15), however, the magnitude was overpredicted about 2% by the turbulent potential model. The TKE decaying linearly to zero in the viscous sublayer region was clearly resolved by the present model. Figure 6 shows the non-dimensionalized turbulent dissipation rate. The dissipation remained small in the core region near the channel centerline, then increased monotonically toward the wall. On the edge of viscous sublayer layer, y+ ~ 10, the DNS data showed that the dissipation rate jumped to a slightly higher level, instead of increasing continuously. This jump was captured by the turbulent

6

American Institute of Aeronautics and Astronautics

potential model, however, the location of the jump was overpredicted by about 1%. Both DNS data and the current model results indicated the dissipation rate increased linearly in the viscous sublayer toward the wall, which is a source of generating turbulent dissipation. On the wall, the turbulence model overpredicted the dissipation by about 15%. The discrepancy could be a result of the wall boundary condition used for the epsilon equation, which is arguably the most difficult part to model. At the present moment, there is no good experimental data, numerical model or estimate for the turbulent dissipation at a wall.
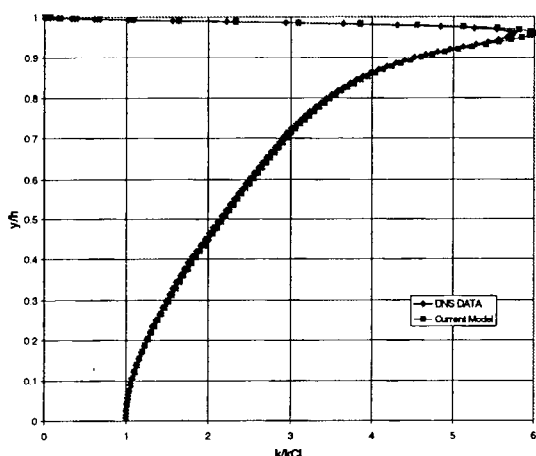
Figure 5. Turbulent kinetic energy profile compared to DNS data.
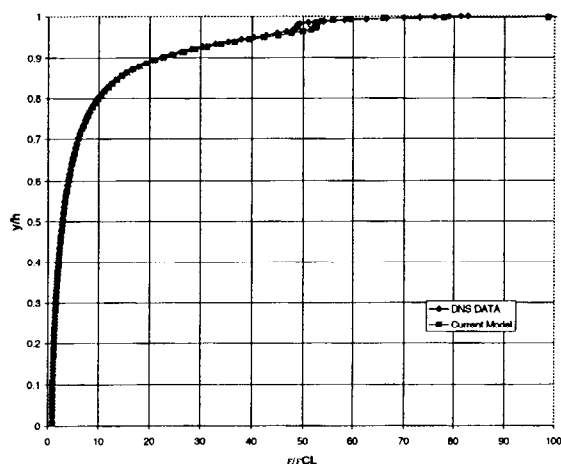
Figure 6. Turbulent dissipation rate profile compared to DNS data.

The next two figures demonstrate the predictive capability of the turbulent potential model for second order closure turbulent transport quantities. As stated in the earlier section, the turbulent potential model was derived from the full Reynolds stress model, therefore it possesses the functionality to predict Reynolds stress components, yet avoids the numerical stiffness problem that is always associated with the Reynolds stress model.

Figure 7 represents the non-dimensionalized Reynolds stress component v'v' compared with the DNS data. In the viscous sublayer, the results compared well with DNS data, showing a near linear increase in this region. In the log layer, the peak location and magnitude were being predicted almost precisely. The present model results deviated from the DNS data only near the channel centerline, but the overall agreement is good. Figure 8 shows the comparison for another non-dimensionalized Reynolds stress, u'v'. Among all the comparisons made with DNS data, this is the only turbulent transport quantity that was not compared well with the DNS data. The turbulent potential model consistently overpredicted, by about 5%, from channel centerline to close to the edge viscous sublayer. The peak location was captured; however, the magnitude was larger than the DNS data.

Overall, the computed fully developed turbulent channel flow results using the turbulent potential model compare very well with the DNS data, which provided fundamental understanding of the model behavior and performance. Furthermore, detailed examinations of each individual turbulent transport quantities revealed the capability of the turbulent potential model in predicting not only the mean flow but also the local and near wall turbulent flows.
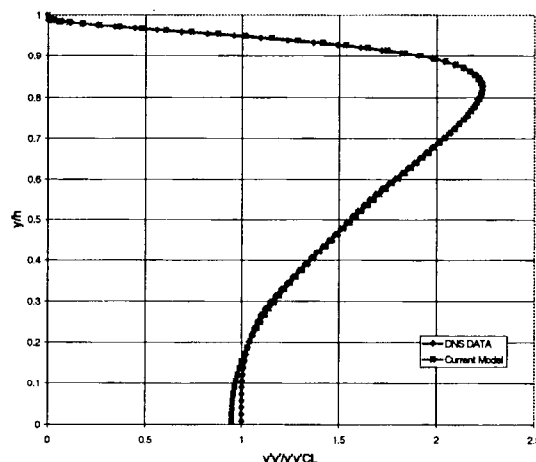

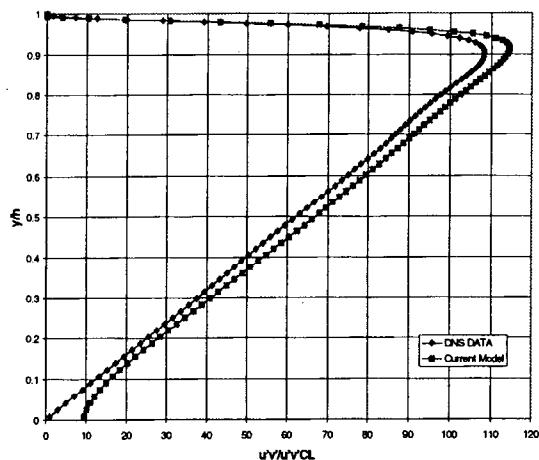Figure 7. Reynolds stress v'v' profile compared to DNS data.

American Institute of Aeronautics and Astronautics

Figure 8. Reynolds stress u'v' profile compared to DNS data.

Figure 10. The overall view of the annular diffuser test rig.

Validation Against Annular Diffuser Laser Velocimetry Data

Annular Diffuser Rig Setup and Test Results

This axisymmetric rig is attractive for a proof-of-concept effort because it provides a flow field which exhibits some key turbulent characteristics while remaining simple enough to be reasonably assumed 2D. A cross section of the annular diffuser rig used is shown in Figure 9. This rig consists of a bellmouth-type inlet leading to a simple annular diffuser that dumps into an exhaust plenum. This existing rig was designed at Concepts, ETI, Inc. (CETI) with full instrumentation capabilities, including windows for laser velocimetry (LV) measurements. Figures 10 and 11 show the overall view and the close-up view of the annular diffuser test rig.
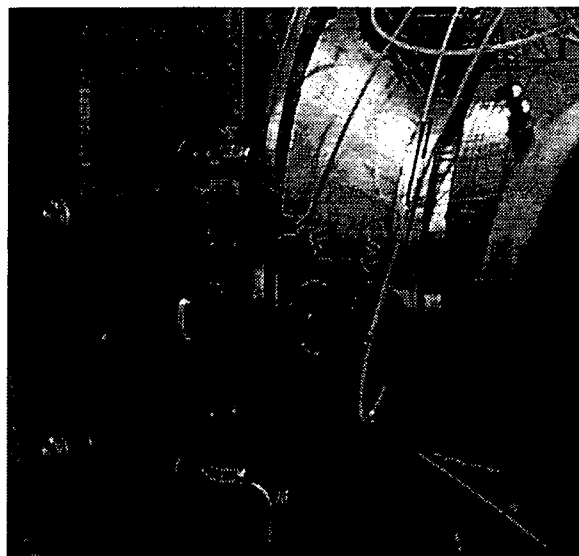

Figure 11. The close-up view of the annular diffuser. The flow enters the diffuser from right to left.

With the rig as configured, it will be possible to take complete LV traverse measurements across the passage at several stations. The purpose of this test is to use LV techniques to resolve a series of fundamental turbomachinery flow field phenomena, where the flow is under the influence of curvature (rotation), adverse pressure gradient (diffusion), and laminar-to-turbulent transition. This sophisticated, yet straightforward test accomplishes all of these objectives and will provide key validation data for the 2D compressible model. Note that CFD codes and the associated turbulence models must be able to calculate flows in this simple geometry if flows in more complex turbomachinery geometries are to be predicted.

Figure 9. Cross-sectional view of annular diffuser rig.

8

American Institute of Aeronautics and Astronautics

The tests were run at two different flow rates: a high flow rate of 1.26 kg/s and a low flow rate of 1.01 kg/s. The tests were conducted at room temperature and atmospheric pressure. The L2F traverse data, in the spanwise direction for total velocity at two stations, as indicated in Figure 9, were collected. The spanwise data traverses were plotted to show the velocity profiles at these two measurement stations in Figures 12 and 13 for the high and low flow rate cases, respectively.
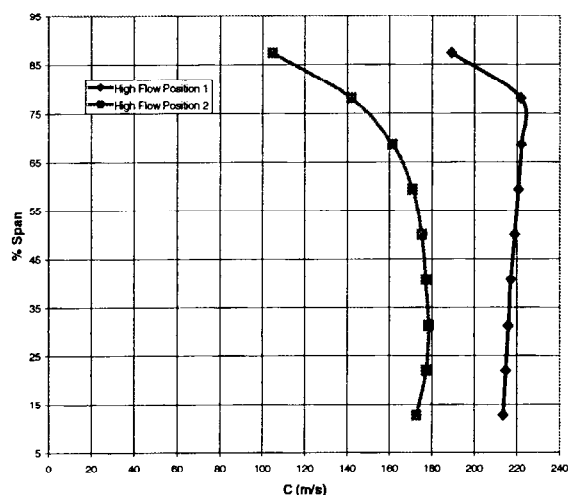

Figure 12. Measured L2F velocity profile for the high flow rate case.
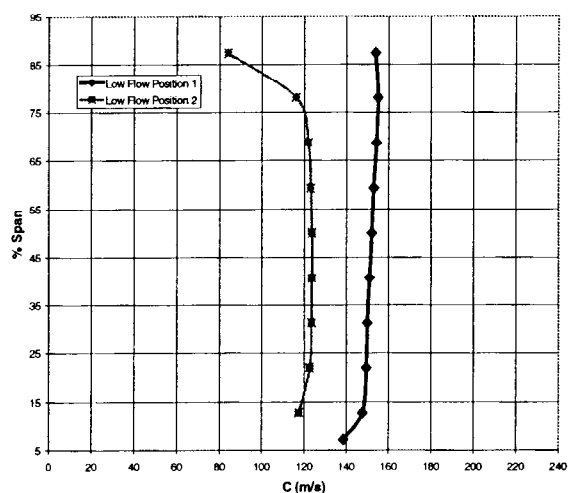
Figure 13. Measured L2F velocity profile for the low flow rate case.

Computational Results

The computational results using the algebraic Baldwin-Lomax turbulence model, the two equation k-ε model and the turbulent potential model are presented in this section. The computational mesh was 101 x 101 for the

annular diffuser, as shown in Figure 14. The mesh is stretched on both the hub and shroud side of the annular diffuser to provide grid resolution in the viscous sublayer for the near wall turbulence behavior. This enables the accurate prediction of turbulent production and dissipation rate, and therefore, leads to a more accurate Reynolds stress calculation for higher order closures. The mesh was uniformly distributed in the throughflow direction. The flow entered in the annular diffuser from left to right, then turned by the 45° bend, then moved up in the radial direction. As radius increases, the cross-sectional area increases. This provides an adverse pressure gradient environment for the flow. In addition, the turning serves the purpose of providing the mechanism of rotation. The inlet boundary conditions for the computation were assumed to be the room temperature and atmospheric pressure, without swirl. The freestream turbulence intensity level is set to be 1%.
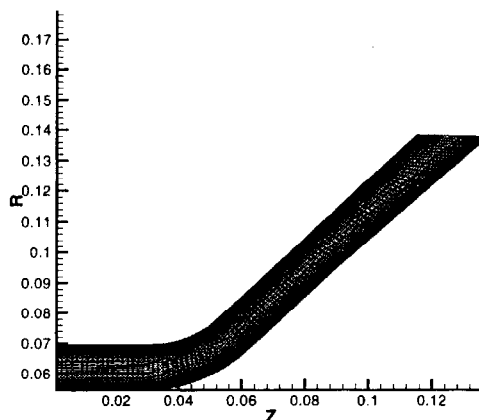

Figure 14. The computational mesh for the annular diffuser. The mesh size is 101 x 101.

The representative computational results for the high flow rate case using the turbulent potential model are presented in the following. The Reynolds number based on the channel height is about 250,000. Figure 15 shows the total velocity contours. For the high flow case, the flow speed at the inlet is about 220 m/s, accelerates around the corner to 240 m/s, enters the diffusing section of the channel and slows down gradually, then exits the annular diffuser at about 100 m/s. The low momentum region (with lower velocity) near the shroud line, after the turning of the diffuser, has been observed. This phenomenon, associated with the adverse pressure gradient, resembles the general flow field in a centrifugal compressor and accelerates around the bend to cause local pressure drop to a minimum value of 60 KPa in this region. The exit gives a very good indication for the validation effort. Figure 16 represents the static pressure contours in the

American Institute of Aeronautics and Astronautics

annular diffuser. This figure clearly shows the adverse pressure gradient throughout the diffuser, with exception of the region around the turning corner. The local flow field static pressure is about 91 KPa for the high flow rate case. These two figures represent the global flow field phenomenon.
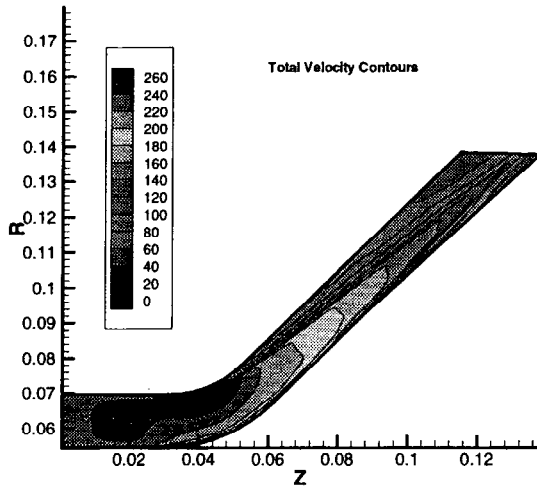
subsequent low momentum and its associated stronger velocity gradient along the shroud line, the TKE magnitude is obviously seen larger than at the hub region. The TKE penetration into the core region can also be observed. In the core region, the TKE remains at a low level until the flow exits the diffuser. A similar trend can be found in the turbulent dissipation rate contours, as shown in Figure 18.

Figure 15. Total velocity contours in the annular diffuser for the high flow rate case.
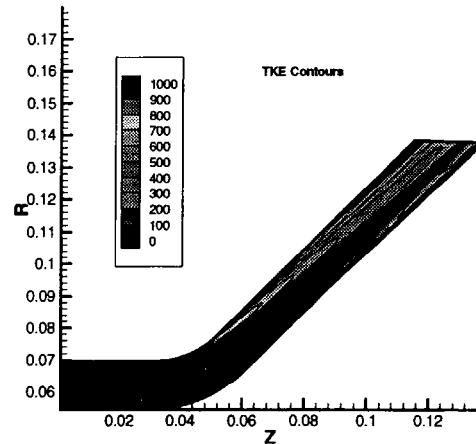

Figure 17. Turbulent kinetic energy contours in the annular diffuser for the high flow rate case.

Figure 16. Static pressure contours in the annular diffuser for the high flow rate case.

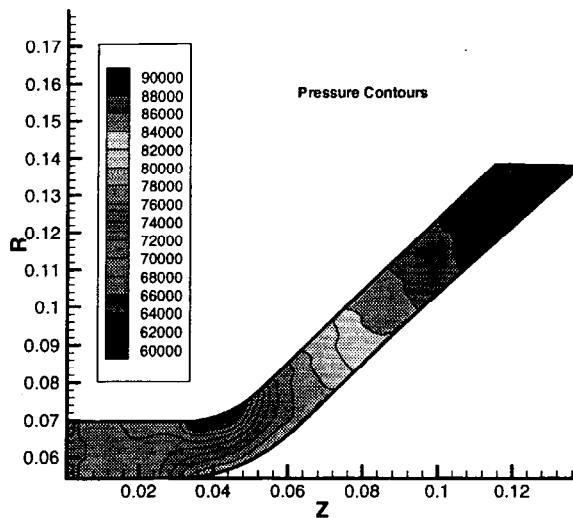Figure 18. Turbulent dissipation rate contours in the annular diffuser for the high flow rate case.

Figure 17 shows the turbulent kinetic energy contours, while Figure 18 depicts the turbulent dissipation rate contours. In Figure 17, turbulent kinetic energy was generated close to both the hub and the shroud of the annular diffuser due to the specific velocity gradient near the wall. Because of the turning and the
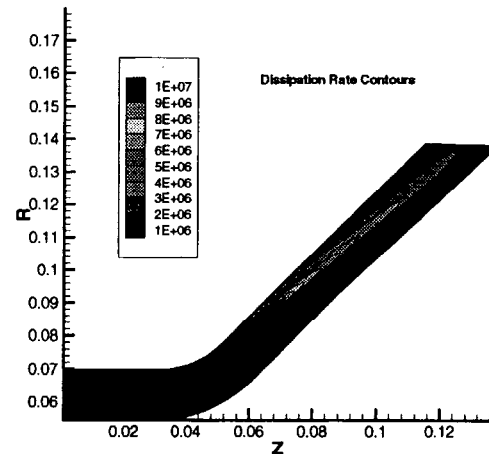
Two Reynolds stress components, v'v' and u'v' are presented in the next two figures. For a two-dimensional flow, these components represent the dominant second order quantities. Figure 19 shows the v'v' contours. This figure is similar to the TKE contours, since the production of this Reynolds stress component is proportional to turbulent kinetic energy. Large concentrations of v'v' near the turning region and

American Institute of Aeronautics and Astronautics

the shroud line can clearly be observed. In Figure 20, the contours of u'v' is shown. Note that the production of this Reynolds stress component is related to the mean vorticity of the flow field. For a channel flow, the vorticity goes from negative in the bottom half of the channel due to negative velocity gradients, to zero at the centerline, to positive in the upper half of the channel because of positive velocity gradients. Therefore, the u'v' contours shows exactly the same phenomenon as the vorticity for a channel flow. In Figure 20, at the diffuser inlet, it is seen that the zero contour line divides the channel in half. Then the zero contour line starts to deviate from the centerline of the diffuser channel, depending upon the local vorticity field of the flow. Despite its sign, the magnitude of the u'v' contours remains low in the core region, while being strong near the wall boundaries. The diffusion of these Reynolds stress components into the core region, as well as downstream locations, were observed in both Figures 19 and 20. This agrees with the other computed turbulent quantity contours and the global diffuser flow phenomenon.

Detailed examination of the computational results for the low flow rate case reveals a similar turbulent flow pattern for both the global flow field and the detailed turbulent transport quantities. These contours for the low flow rate case will be included here for simplicity. The computed results, however, will certainly be presented in the following section to compare with the L2F test data.
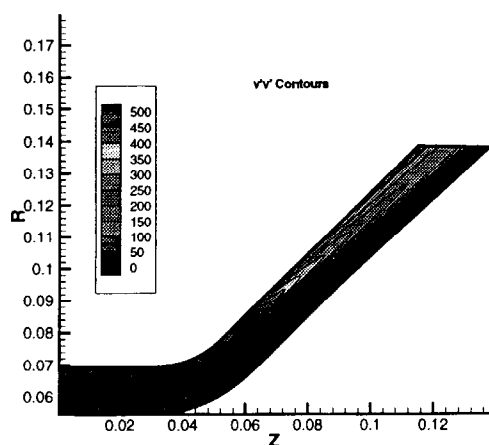

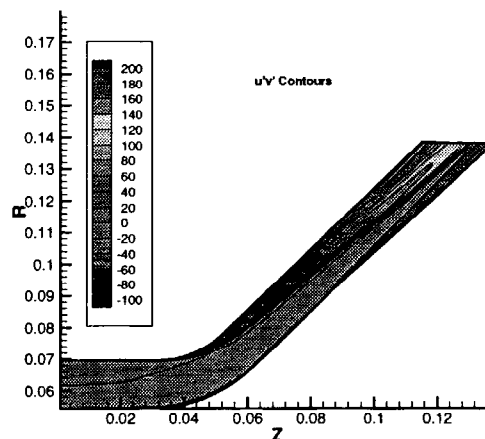Figure 19. Reynolds stress component v'v' contours in the annular diffuser for the high flow rate case.

Figure 20. Reynolds stress component u'v' contours in the annular diffuser for the high flow rate case.

Note that the Reynolds numbers for both the high flow rate case (250,000) and the low flow rate case (175,000) are large enough to impose numerical stiffness and model infidelity for a number of turbulence models. Very often a number of modeling constants in these turbulence models, for example the two equation k-ε model, need to be tweaked to produce results for a particular case. The tried-and-error procedure was a standard practice for most of the existing turbulence models. During the course of using the turbulent potential model, all the modeling constants remained unchanged, i.e., without being tweaked to achieve the computational results. Furthermore, the BTOB3D turbomachinery CFD code converged without encountering numerical stiffness or instability, when running the turbulent potential model.

Comparisons with L2F Data

As indicated in Figure 10, the L2F data traverses were taken at two stations. The first data station is located immediately downstream of the 45° bend, when both the hub and shroud curvatures return back to zero. The second data traverse is about halfway through the diffusing section of the diffuser channel path. The data taken at these two stations are far enough away from the diffuser exit, that downstream exhaust distribution should have no effect on the measured quantities. The computational results at these two locations are compared with the L2F data for both the high and low flow rate cases. We will begin comparisons and discussions with the low flow rate case, which has a moderately high Reynolds number of 175,000.

There are three turbulence models used in this validation study: the algebraic Baldwin-Lomax model,

11

the two-equation k-ε model, and the current turbulent potential model. Note that all three models are implemented into the BTOB3D turbomachinery CFD code, sharing the same numerical algorithm and the same numerical dissipation characteristics. Therefore, there is no bias in this study towards a particular turbulence model, nor as to whether to use one turbulence model from one CFD code, and another model from another CFD code. In this manner, the comparisons made with data using the three turbulence models become meaningful.

Figure 21 shows the comparisons with measured velocity profile at the first data traverse station, while Figure 22 represents the comparisons at the second data location. As can be seen in Figure 21, generally speaking, all three turbulence models used predicted velocity profiles that are relatively close to the measured data at this location. The Baldwin-Lomax model underpredicted the velocity profile consistently by less than 5% throughout the span. The k-ε model agreed with the data well from hub to about 30% span, then deviated from data slightly, overpredicted by less than 3%. The turbulent potential model showed a slightly better result than the k-ε model, by agreeing with the data from hub to about 60% span location, then overpredicted the near shroud flow by less than 2%.
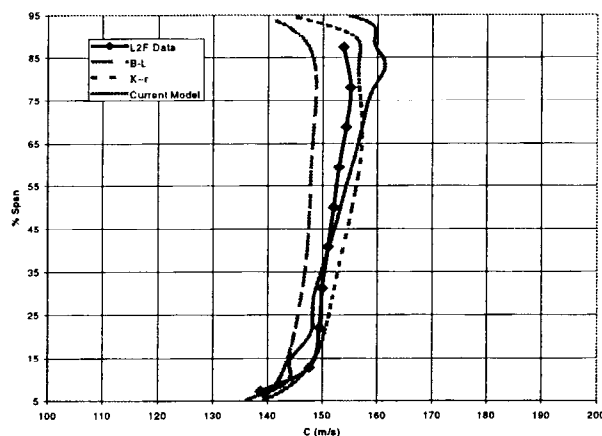

Figure 21. Comparison with L2F data at the first data traverse location for the low flow rate case.

In Figure 22, at the second data station, the Baldwin-Lomax model underpredicted the velocity profile further, the velocity magnitude being 10% lower than the measured data. This is understandable, because at a further downstream location, more turbulent transport processes (production, dissipation, etc.) should have

happened. The isotropic turbulence, inner-outer layer matching assumption, without the consideration of adverse pressure gradient, curvature (rotation), and the diffusion effects, the algebraic Baldwin-Lomax model simply misrepresented the complicated turbulent transport phenomena in the annular diffuser channel. Both the k-ε and the turbulent potential models predicted nearly the same results from hub to about 60% span location, however, both undepredicted by about 5% compared to data. From 60% to about 80% span, the turbulent potential model outperformed k-ε model by almost agreeing with the measured data, while the k-ε model underpredicted by 10%. Finally, all three models overpredicted the data point at 88% span location by at least 25%. The measured velocity indicated a more significant diffusion process occurred at this span location and all the turbulence models did not come close to what was measured. This misprediction might suggest that, in reality, the turbulent flow might be more strongly coupled with the adverse pressure gradient and curvature than the presently available models can handle.
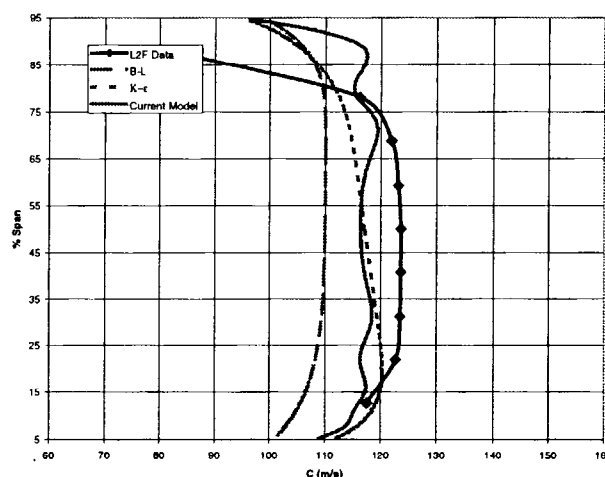

Figure 22. Comparison with L2F data at the second traverse location for the low flow rate case.

Comparisons with the measured data for the high flow rate case are presented in Figures 23 and 24. At the first data traverse location, which is shown in Figure 23, the Baldwin-Lomax model overpredicted the velocity profile by about 10% consistently for most of the span. Near the shroud line, the 88% span data point showed that Baldwin-Lomax model overpredicted close to 20%. On the contrary, the k-ε model consistently underpredicted the velocity profile by 7% compared to data. The 88% span data point was again greatly missed by the k-ε model. However, the two equation

American Institute of Aeronautics and Astronautics

k-ε model results did indicate a better agreement than the Baldwin-Lomax model. The turbulent potential model showed amazingly good agreement with the L2F data, from hub to about 80% span location, with several data points falling on the predicted profile. Furthermore, the turbulent potential model predicted exactly the 88% data point; however, the predicted results showed a stronger velocity gradient from 80% to 88% span compared to the measured data. At this data location, it is clear that the turbulent potential model captured the correct flow characteristics, while Baldwin-Lomax and k-ε models did not agree well with data, by mispredicting both the core flow and boundary layer velocity gradients.

flow in the near wall region. Figure 24 clearly shows this trend of the k-ε model. On the other hand, the present turbulent potential model predicted an excellent velocity profile compared to the data, from hub to about 50% span location. In this region, the computational results agreed with the data very closely. In addition, as shown in the previous figure, the turbulent potential model predicted the velocity at 88% span location almost precisely. However, a stronger velocity gradient in the near wall region was still observed compared to the measured data. The turbulent potential model has shown a promising potential to predict turbulent flow in turbomachinery, yet can be improved in the near wall modeling portion of the model.

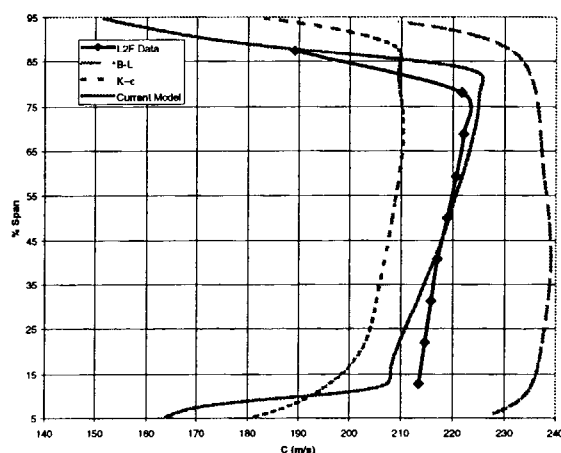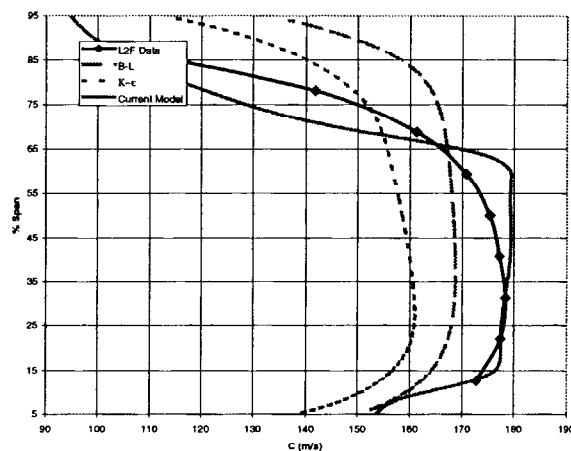Figure 23 Comparison with L2F data at the first data traverse location for the high flow rate case.

Figure 24. Comparison with L2F data at the second traverse location for the high flow rate case.

At the second data station, as indicated in Figure 24, the L2F data represented a thick boundary layer, possibly due to curvature and adverse pressure effects from the 60% span location to the shroud line. In this figure, both Baldwin-Lomax and k-ε models underpredicted the measured velocity profile. Combining with the first data location prediction, the Baldwin-Lomax model did not provide a consistent predictive trend (overpredicting at location 1, while underpredicting at location 2). For complicated turbulent flow physics like the annular diffuser, therefore, the Baldwin-Lomax model cannot be counted on to provide a reliable solution. The k-ε model consistently underpredicts the velocity profile in the core region at both locations. This seemed like a step increase compared to the Baldwin-Lomax model. Judging from the k-ε results, the signature 'strong dissipation' characteristics prevailed again, to lead to fast penetration of TKE from the boundary layer to the core region. As a result, the model likely underperdicts the mean flow in the core region, while overpredicts the

Combined with the finding in the previous figure, the result has shown that the turbulent potential model has successfully captured the complicated turbulent transport phenomenon for this diffuser flow field. In other words, the turbulent potential model predicted a realistic transport of TKE, dissipation, and other second order turbulent closure quantities, from their source of generation (the near wall region) to the mean flow area (core region). The two most popular turbulence models, the algebraic Baldwin-Lomax and the two equation k-ε models, did not reach close agreement with the L2F data for the annular diffuser flow field, which can be considered to be a representative turbomachinery flow field. *Turbulence models, need to show good agreement with data for this simplified annular diffuser flow field before they can be applied to accurate and realistic turbomachinery flow predictions.* After conducting this validation study, it is clear *the turbulent potential model outperformed both the Baldwin-Lomax and the k-ε models* by predicting more accurate results

13
American Institute of Aeronautics and Astronautics

when compared to the L2F data, for both the low and high flow rate cases, without tweaking any modeling constants for these two high Reynolds number flows. This achievement is a step increase in turbulence modeling capability for complicated turbomachinery flow fields.

SUMMARY

The development and validation of the turbulent potential model has demonstrated a clear start towards developing a comprehensive turbulence model, not only for turbomachinery, but for all aspects of turbulent flow field applications. Progress has been made on developing the 2D compressible flow model, particularly for turbomachinery flows, integration into the BTOB3D turbomachinery CFD solver supported by an annular diffuser rig test with L2F test data for validation. A series of supplementary validation studies using the turbulent potential model against classical turbulent flow bench mark cases, including DNS data, was also given. The validation results clearly indicate that the turbulent potential model surpasses two widely used turbulence models, the Baldwin-Lomax model and the two equation k-ε model. CETI will continue this work for further advancement of this much needed technology.

ACKNOWLEDGMENT

REFERENCES

1. Hirsch, C., "CFD Methodology and Validation for Turbomachinery Flows," AGARD Lecture Series on Turbomachinery Design Using CFD, 1994.

2. Baldwin, B., and Lomax, H., "Thin Layer Approximation and Algebraic Model for Separated Turbulent Flow," AIAA 78-0257, 1978.

3. Dawes, W. N., "The Development of a Solution Adaptive 3D Navier-Stokes Solver for Turbomachinery," AIAA 91-2469, 1991.

4. Nakahashi, K., Nozaki, O., Kikuchi, K., and Tamura, A., "Navier-Stokes Computations of Two- and Three-Dimensional Cascade Flow Fields," AIAA 87-1315, 1987.

5. Launder, B. E., and Spalding, B., "Mathematical Models of Turbulence," Academic Press, 1972.

6. Hah, C., "Numerical Solution of Three-Dimensional Flows for Modern Gas Turbine Components," ASME 87-GT-84, 1987.

7. Matuso, Y., "Computations of Three-Dimensional Viscous Flows in Turbomachinery Cascades," AIAA 91-2237, 1991.

8. Jennions, I. K., and Turner, M. J., "Three-Dimensional Navier-Stokes Computations of Transonic Fan Flow Using an Explicit Flow Solver and an Implicit k-ε Solver," ASME 92-GT-309, 1992.

9. Savill, A. M., "Evaluating Turbulence Predictions of Transition - an ERCOFTAC SIG Project," Advances in Turbulence, Nieuwstadt Ed. pp. 555. Kluwer Academic Publishers, 1992.

10. Leschziner, M. A., and Launder, B. E., Eds., Proceedings of the 2nd ERCOFTAC-IAHR Workshop on Refined Flow Modeling, Univ. of Manchester, UK, 1993.

11. Mansour, N. N., Kim, J., & Moin, P., "Reynolds-Stress and Dissipation-Rate Budgets in a Turbulent Channel Flow," J. Fluid Mech. Vol. 194, pp.15-44, 1988.

12. Perot, J. B., AND Moin, P., "Shear-free turbulent boundary layers. Part 2. New concepts for Reynolds stress transport equation modeling of inhomogeneous flows". J. Fluid Mech., Vol. 295, pp. 229-245, 1995.

13. Perot, J.B., "A New Approach to Turbulence Modeling," SBIR Phase I Final Report," Aquasions, Inc., 1997.

14. Dawes, W. N., "A Computer Program for the Analysis of Three-Dimensional Viscous Compressible Flow in Turbomachinery Blade Rows," Whittle Laboratory, Cambridge, UK, 1988.

15. Johnson, D. A., and King, L. S., "A Mathematically Simple Turbulence Closure Model for Attached and Separated Turbulent Boundary Layers," AIAA J. vol. 23, pp. 1684-1692, 1985.

16. Bradshaw, P., Ferris, D. H., and Atwell N. P., "Calculations of Boundary-Layer Development Using the Turbulent Energy Equation," J. Fluid Mech., vol. 28, pp. 593-616, 1967.

17. Samual, A. E., and Joubert, P. N., "A Boundary Layer Developing in an Increasingly Adverse Pressure Gradient," J. Fluid Mech. vol. 66, pp. 481-505, 1974.

18. Moser, R. D., Kim, J., and Mansour, N. N., "Direct Numerical Simulation of Turbulent Channel Flow up to $Re = 590$", Physics of Fluids, Vol. 11, 1999.